

Journal of
**Micro/Nanolithography,
MEMS, and MOEMS**

Nanolithography.SPIEDigitalLibrary.org

Effects of wafer noise on the detection of 20-nm defects using optical volumetric inspection

Bryan M. Barnes
Francois Goasmat
Martin Y. Sohn
Hui Zhou
András E. Vladár
Richard M. Silver

Effects of wafer noise on the detection of 20-nm defects using optical volumetric inspection

Bryan M. Barnes,* Francois Goasmat, Martin Y. Sohn, Hui Zhou, András E. Vladár, and Richard M. Silver

National Institute of Standards and Technology, Semiconductor and Dimensional Metrology Division, 100 Bureau Drive MS 8212, Gaithersburg, Maryland 20899-8212, United States

Abstract. Patterning imperfections in semiconductor device fabrication may either be noncritical [e.g., line edge roughness (LER)] or critical, such as defects that impact manufacturing yield. As the sizes of the pitches and linewidths decrease in lithography, detection of the optical scattering from killer defects may be obscured by the scattering from other variations, called wafer noise. Understanding and separating these optical signals are critical to reduce false positives and overlooked defects. The effects of wafer noise on defect detection are assessed using volumetric processing on both measurements and simulations with the SEMATECH 9-nm gate intentional defect array. Increases in LER in simulation lead to decreases in signal-to-noise ratios due to wafer noise. Measurement procedures illustrate the potential uses in manufacturing while illustrating challenges to be overcome for full implementation. Highly geometry-dependent, the ratio of wafer noise to defect signal should continue to be evaluated for new process architectures and production nodes. © The Authors. Published by SPIE under a Creative Commons Attribution 3.0 Unported License. Distribution or reproduction of this work in whole or in part requires full attribution of the original publication, including its DOI. [DOI: [10.1117/1.JMM.14.1.014001](https://doi.org/10.1117/1.JMM.14.1.014001)]

Keywords: wafer noise; defect inspection; volumetric processing; defect metrology; three-dimensional image processing.

Paper 14115P received Jul. 18, 2014; accepted for publication Dec. 11, 2014; published online Feb. 11, 2015.

1 Introduction

Optical methods are instrumental for patterned defect inspection in semiconductor fabrication, as the quality of these measurements directly affects the manufacturing yield. Optical imaging is inherently parallel and thus covers relatively large areas quickly compared with scanning techniques, leading to higher throughput. However, the International Technology Roadmap for Semiconductors (ITRS) shows that ever-decreasing sizes of features and spaces in these patterns have strained the capabilities of optical tools to differentiate between patterning defects and false positives. The ITRS also reports that there are currently no known solutions for achieving desired processing speeds and capture rates.¹ In addition, it can be shown that as dimensions decrease, “killer defects” will eventually scatter light² as Mie scatterers, having intensities effectively proportional to d^6/λ^4 (where d is the diameter of the scatterer and λ is the wavelength of light) exacerbating the ongoing challenge of maintaining a sufficient signal-to-noise ratio (SNR).

We have recently developed a new, three-dimensional (3-D) volumetric defect inspection method for mitigating the effects of random noise while using the continuity of the defect to bolster defect detection.^{3,4} Volumetric processing of the full 3-D scattered field is not restricted to focus-resolved imaging as is shown here; angle-resolved sampling of the 3-D scattered field can be similarly processed. Optical images are collected and data analysis is performed to yield (x, y, z) indexed volumes of reflected light intensity data. The goal of this method is to separate measured intensities

due to defects from all other intensities. A brief review of the volumetric technique follows in the next section.

These other intensities, which can lead to false positives and large reductions of the SNR, originate generally either from the instrument or from wafer noise, defined below. Examples of instrument-based sources of imaging noise include the shot noise of the charge coupled device, the stray light and glare within the optical columns, and intensity inhomogeneities across the field of view from misalignment, lens imperfections, aberrations, and laser speckle. These sources of error can be significant but are reduced as much as practicable through optical design and design of experiment. In our measurements, speckle is partially removed by using a rotating diffuser at the source plane while aberrations have been reduced through design optimization. Furthermore, systematic instrumental noise effects are largely mitigated by collecting “defect” and (after wafer shifting) “reference” sets of images for differential analysis under nearly the same experimental conditions. These procedures, coupled with a volumetric approach that reduces the effects of random noise, permit a more thorough exploration of the effects of wafer-based intensity noise relative to the defect.

Wafer noise is observed as scattering from the sample of interest due to its physical variations such as line edge roughness (LER) and line width roughness (LWR), as well as possible materials variation.^{2,5} In many ways, the optical scattering behavior of wafer noise should mimic that of patterned defects. Wafer noise should be observable over an extended focal range. It should persist in differential imaging as the LER and LWR do not overlap between the “defect” and “reference” acquisitions. This paper studies the degree to which wafer noise qualitatively and quantitatively impacts defect detection using a through-focus volumetric approach with both simulated and experimental data presented.

*Address all correspondence to: Bryan M. Barnes, E-mail: bmbarnes@nist.gov

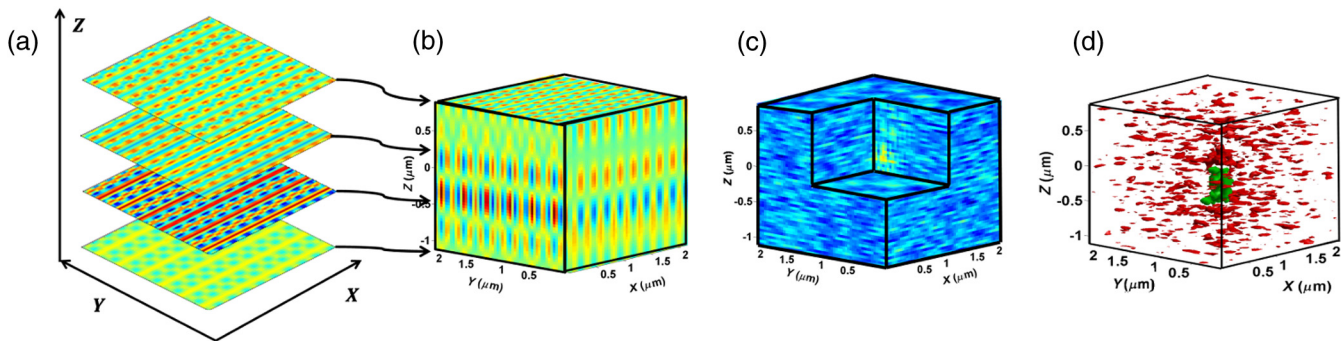


Fig. 1 Schematic of three-dimensional (3-D) volumetric processing: (a) Images from a defect are collected or simulated through focus. (b) These images can be transformed into a volume of intensity information. Likewise, a reference volume can also be obtained. (c) The defect and reference volumes are subtracted yielding a differential volume. A cut out shows the defect within. (d) Intensity and spatial extent thresholding yields the large central subvolume (green) in the center due to a defect, and the remaining subvolumes are noise (red).

2 Optical Three-Dimensional Volumetric Processing

Although optical focus-resolved 3-D volumetric defect detection has been described in depth elsewhere,^{3,4} it is important to reiterate the required steps to better explain the results presented. A schematic of the process is shown as Fig. 1 using a simulation example. Sets of images of a defect are collected at various focus positions. These images are treated as xy slices of an xyz volume of intensities that can be constructed from these images, shown in Fig. 1(b). Repeating the process using a defect-free or defect-shifted sample yields a “reference” volume similar to the “defect” volume. Experimental volumes often require Fourier filtering and correlation,⁶ both performed in three dimensions. The reference and defect volumes can be subtracted to yield a differential volume as shown in Fig. 1(c). In this schematic, a strong signal from the defect is observable in the center as shown in the cut out. For this illustration, random and correlated noises have been added to the difference volume after processing; elsewhere in this paper, wafer noise originates from the scattering off noisy samples and no additional imaging noise has been added. To produce Fig. 1(d), the differential data are converted to absolute values and thresholded using a minimum intensity, creating several subvolumes. By filtering the 3-D spatial extent of these subvolumes, the scattering due to the defect can be identified in the center of Fig. 1(d), with the noise subvolumes scattered all around.

Measured differential volumetric image data from two different dies are shown as Fig. 2 to further illustrate this methodology and to illustrate questions to be addressed in this paper. Due to wafer shifting to obtain the “reference” volume, there are two copies of the defect visible in each panel of the figure. Specifically, two elongated subvolumes in Fig. 2(a) are due to the presence of a defect, with the remaining subvolumes attributable to noise. In Fig. 2(b), which was first presented in Ref. 4, there are a greater number of nondefect subvolumes. The greater amount of noise stems from at least two sources. First, the die imaged in Fig. 2(a) is known from scanning electron microscopy (SEM) to have more optimal patterning than the die optically imaged in Fig. 2(b). Second, the data for Fig. 2(b) were accumulated using a different illumination configuration that

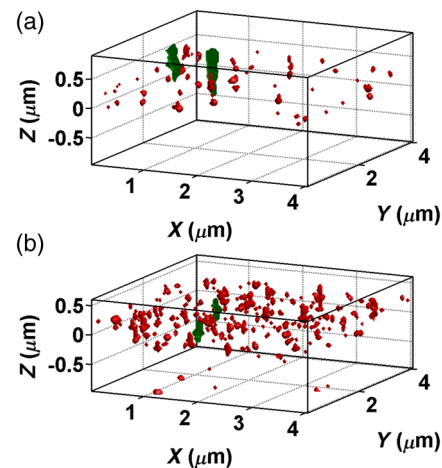


Fig. 2 Two examples of volumetrically processed through focus differential images. (a) Bridging defect imaged differentially with full-field illumination. (b) Similar bridging defect on a different die imaged with dipole illumination, reprinted from Ref. 4. These defect volumes can be visualized after thresholding, colored green online. Data subvolumes colored red online are noise.

yields less light compared with Fig. 2(a). It is important to isolate whether or not this added noise can be attributed to an increase in wafer noise. In addition, it is important to monitor whether the defect optical signature extends through a longer focal z -range than the noise. Stated differently, could wafer noise be expected to have an extent in z as large as a defect? To address these questions, two simulation studies are presented to compare the optical scattering behavior of samples with LER, LWR, and imperfections relative to the optical scattering from intentionally patterned defects. Measurements on a well-patterned die and the same imperfectly patterned die from Fig. 2, under the same illumination conditions, yield a systematic evaluation of wafer noise.

3 Simulation Studies with Wafer Noise

Two separate simulation studies were performed, both based upon the SEMATECH 9-nm intentional defect array (IDA). (Certain commercial materials are identified in this paper in order to specify the experimental procedure adequately. Such

identification is not intended to imply recommendation or endorsement by the National Institute of Standards and Technology, nor is it intended to imply that the materials are necessarily the best available for the purpose.) Each study employs the electromagnetic scattering simulations using a finite-difference time-domain (FDTD)⁷ solver at $\lambda = 193$ nm, the measurement wavelength. In the first study, LER was applied to the IDA design layout to determine the spatial extent of wafer noise and the extensibility of volumetric methods to 9-nm critical dimensions (CDs). Transverse-electric (TE) and transverse-magnetic (TM) linearly polarized plane waves were simulated and volumetrically processed individually to determine the optimal polarization and azimuthal angle for each defect with respect to its SNR. By enhancing the incident illumination for greater sensitivity, the effects of wafer noise on sensitivity are more readily identified. For the second study, structures on a patterned IDA wafer were measured using SEM with images transformed into inputs to the scattering simulation. Multiple plane waves were computed to replicate the finite aperture of our experimental apparatus and results were combined to form each volumetric image. This exercise yields a more realistic comparison to the experimental measurement as the inherent LER, LWR, and patterning imperfections of the IDA are better represented in the simulation. In both studies, the primary concentration was on the “Bx” and “By” bridging defects which connect the line segments orthogonally as shown in Fig. 3.

In this work, three thresholds are used to identify potential defects in volumetric differential images. The intensity (I) thresholds for the simulation studies are scaled relative to the standard deviation (σ_I) of the absolute value of each differential image. An alternative, valid approach for comparative defect evaluation would be to set the threshold proportional to the incident light I_0 . While such a fixed threshold is applicable to simulations, it is challenging to actively employ fixed intensity thresholding on filtered measured data. Thus, in this work, relative thresholds were maintained throughout for consistency. Volumetric pixels (voxels) above the intensity threshold must next meet continuity requirements with other voxels to be included in a subvolume. Finally, a spatial

extent threshold assesses the size of the smallest box—the “bounding box”—that would contain each subvolume. The minimum bounding box for a defect subvolume was set to $100 \text{ nm} \times 100 \text{ nm} \times 600 \text{ nm}$. Further optimization and combination of thresholds can be performed to maximize the sensitivity to the defect signals within a given four-dimensional dataset.

Both studies used the same defect metric and estimator for the SNR. The defect metric here is the sum of the absolute intensities in the defect subvolume(s). The SNR requires a more in-depth discussion. From one perspective, this volumetric data processing method optimally yields two distinct and separable datasets per differential volume: subvolume(s) attributed to the defect and subvolume(s) attributed to the noise. An SNR from that perspective is ill-defined. The introduction of an intensity threshold complicates straightforward approaches to the calculation. Although Poline et al.⁸ have presented statistical treatments for combining spatial extent testing and peak intensity thresholding for assessing the risk of error in analyzing 3-D positron emission tomography images, we construct an estimate for the SNR consistent with the work of McCann et al.⁹ who presented several approaches to determining an SNR for magnetic resonance imaging with regions-of-interest. The mean of the defect subvolume(s), I_{defect} , is the signal, while the standard deviation across the noise subvolume(s), σ_{noise} , is the noise, yielding

$$\text{SNR} \approx \frac{I_{\text{defect}}}{\sigma_{\text{noise}}} \quad (1)$$

This treatment will allow quantitative comparison among the data within a given simulation or measurement dataset.

3.1 First Study: Adding Line Edge Roughness to the Graphic Data System

This first study permits investigation of the effects of wafer noise by applying a well-defined LER to the nominal design of the 9-nm gate IDA through its Graphic Data System (GDS) file. This LER is characterized by its rms roughness, σ_{LER} , and its correlation length, ξ . Simulation inputs were generated using a procedure⁵ laid out by Crimmins for applying a

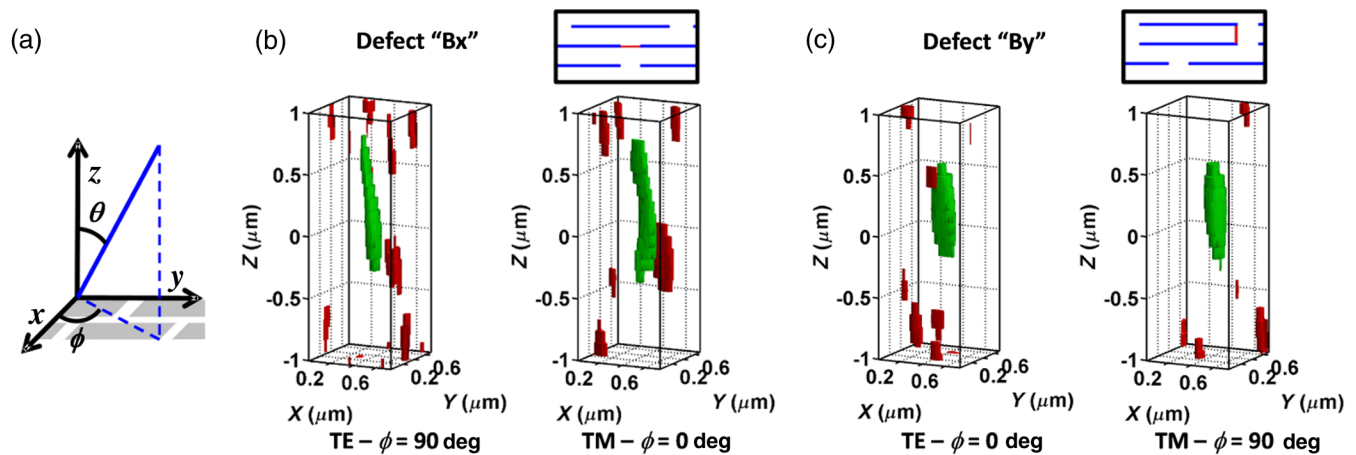


Fig. 3 (a) Definitions for polar (θ) and azimuthal (ϕ) angles in these studies with respect to x , y , and z . (b) Schematics of the “Bx” and (c) “By” defects with volumetric differential images of the two defects for the transverse-electric (TE) and transverse-magnetic (TM) polarizations at the stated azimuthal angle ϕ with polar angle $\theta = 21$ deg from normal incidence. Spherical equivalent volume diameters (SEVD) are 146 and 135 nm for “Bx” and “By,” respectively.

correlation length to a random sequence. The correlation length is invoked using a target autocorrelation function:

$$f(x) = \xi^{1/2} \pi^{-1/4} e^{-\frac{x^2}{2\xi^2}}. \quad (2)$$

This modified random sequence was added to the sides and ends of each line segment within the GDS file including the defect. Specifically, one randomization yielded an LER with $(\sigma_{\text{LER}}, \xi)$ for a defect-free reference, while a separate randomization was used to generate LER with the same magnitude $(\sigma_{\text{LER}}, \xi)$ for the line arrays of the “Bx” and “By” defects. This process ensured a mismatch between the edge geometries of the reference and defect.

Simulation of the LER rms roughness on the subnanometer scale requires multiple assessments of one’s computational capabilities. Values were derived from the ITRS, with an LER rms roughness $\sigma_{\text{LER}} = 0.65$ nm (one standard deviation) obtained from current LWR values (treated as uncorrelated), while assigning $\xi = 8$ nm which is forecasted for a 9-nm dynamic random-access memory $\frac{1}{2}$ pitch.¹⁰ ITRS LER and LWR values are 3σ values, a coverage factor $k = 3$; in this present treatment, σ_{LER} is the 1σ value ($k = 1$). For this study, the rms roughness was not equally forward-looking given the memory requirements and evaluation time required for the FDTD model at these length scales. In an initial assessment, FDTD cubic grid sides were varied from 0.75 to 2.25 nm to test the convergence for $\sigma_{\text{LER}} = 0.65$ nm. A second investigation varied the FDTD domain size from 1×3 unit cells ($0.72 \mu\text{m} \times 0.72 \mu\text{m}$ in xy) up to 4×12 unit cells ($2.88 \mu\text{m} \times 2.88 \mu\text{m}$ in xy). After evaluating tradeoffs among speed, accuracy, and computational capabilities, the domain size used here was 1×3 with a grid size of 1.125 nm, yielding lines 8 grids wide for these 9-nm gate designs.

The defect metric and SNR for the data in Fig. 3 are provided in Table 1. The intensity threshold in this study is $I > 4\sigma_I$. With this threshold, in each case, the defect is easily identified and separable from the wafer noise. Quantitatively, the “By” bridge defect is relatively stronger than that for the “Bx” defect in either linear polarization. (The exact same LER sequence is applied to the nominal patterns for both “Bx” and “By.”) While some wafer noise subvolumes are present in the data, none persist through focus on par with the main defect optical scattering signal. The strongest defect signal is for the TE polarization at the specified azimuthal angles. For the “Bx” defect, TE polarization at $\phi = 90$ deg corresponds to X polarization with respect to the sample, and for “By,” TE polarization at $\phi = 90$ deg corresponds to Y polarization.

As $\sigma_{\text{LER}} = 0.65$ nm yielded wafer noise that left the defect signal largely unperturbed, these simulations were then used as a baseline to evaluate the effects of increasing

the LER rms roughness on defect detectability. Figure 4 displays the portions of the unit cell and defect from the GDS for defect “By,” with LER increasing from left to right, and the data presented illustrate potential difficulties in defect detection with increased LER. Visual comparison of the thresholded volumetric images shows that the wafer noise has a more profound impact as the LER is increased from $\sigma_{\text{LER}} = 0.65$ to 1.95 nm. As the $\sigma_{\text{LER}} = 0.65$ nm case clearly delineates the (x, y, z) position of the defect’s optical scatter and the nominal shape of its subvolume, we can identify not only false negatives, but also “false” positives that are unrelated to the actual defect scattering. Both types of misclassifications are related to wafer noise. In Fig. 4, there is a false negative for $\sigma_{\text{LER}} = 1.95$ nm and an incorrectly positioned “false” positive for $\sigma_{\text{LER}} = 1.63$ nm. The defect scattering was obscured in each case by increased wafer noise. For the “Bx” defect (not shown), $\sigma_{\text{LER}} = 1.30$ nm yields a false negative, while both $\sigma_{\text{LER}} = 1.63$ and 1.95 nm yield similarly shaped “defect” subvolumes completely below the substrate, in stark contrast to the $\sigma_{\text{LER}} = 0.65$ nm case shown in Fig. 3(b).

Table 2 shows the defect metrics, SNR, and $I > 4\sigma_I$ intensity thresholds for both the “Bx” and “By” defects. The SNR for the “By” defect decreases as the LER increases from $\sigma_{\text{LER}} = 0.65$ to 1.30 nm. For $\sigma_{\text{LER}} \geq 1.63$ nm, wafer noise is sufficiently strong to frustrate clear identification of the optical defect signal for either bridge direction. Defect signals misclassified as false negatives or incorrectly positioned false positives are shown in Table 2 with their defect metric and SNR marked with an asterisk (*) to demonstrate that these observed values do not correspond to an actual defect signal.

This simulation study confirms that the wafer noise increases with LER rms roughness and that this wafer noise can be distributed as bright regions of intensity that are located throughout the through-focus volumetric image. Subvolumes of wafer noise for rougher LER samples can be comparable in intensity and spatial extent with the signal from the defect itself. As newer patterning layouts are developed with narrower pitches, smaller line widths, and smaller LER rms roughness, such evaluations will need to be repeated to gauge the relative volume and intensity of the defect signal with respect to the wafer noise as this scattering cannot be overcome by additional measurements at a single plane. In this sense, this study is a first step in evaluating the extensibility and possible necessity of volumetric processing given the challenges of wafer noise.

3.2 Second Study: Scanning Electron Microscopy Data in the Finite-Difference Time Domain

However, achieving a fuller understanding through simulation of the measured experimental data presented earlier as Fig. 2 and subsequently in Sec. 4 may be achieved through

Table 1 Defect metric and signal-to-noise (SNR) estimates for the 9-nm gate intentional defect array (IDA) with $\sigma_{\text{LER}} = 0.65$ nm.

	Bridge “Bx”		Bridge “By”	
	TE – $\phi = 90$ deg	TM – $\phi = 0$ deg	TE – $\phi = 0$ deg	TM – $\phi = 90$ deg
Def. Int. $> 4\sigma$	3952	3500	8585	7979
SNR	18.6	9.3	18.9	16.6

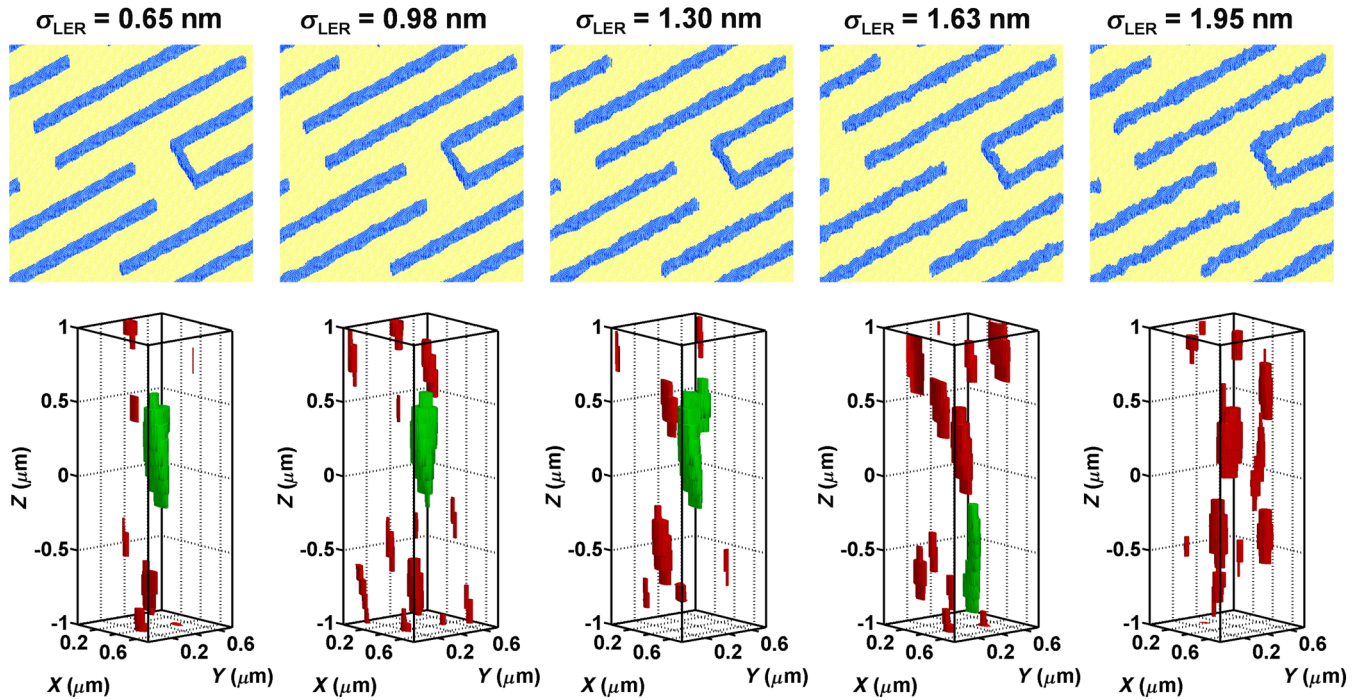


Fig. 4 Differential volumetric analysis for the “By” defect using TE polarization, $\theta = 21$ deg, $\phi = 0$ deg for five different line edge roughness (LER) rms roughnesses. The defect is correctly identified for $\sigma_{\text{LER}} \leq 1.30$ nm.

use of the as-printed layout, which varies from its original design. The second simulation study compares the wafer noise scattered from the SEMATECH 9-nm gate IDA by using SEM data to define the simulation geometry. Instead of relying upon the nominal design from the GDS file as modeling input, the simulation was based entirely upon SEM images acquired from two specific dies on the IDA chosen for their relative patterning quality. For each die, images of the “Bx” and “By” defects were collected, then correlated, and cropped to 3×4 unit cells with the defect near the center of the image. A third cropped image for each die was taken from the periphery of the image of the “By” defect as a reference defect-free pattern. These six images in all were converted using intensity thresholding from grayscale SEM images to binary masks.

For these normalized SEM images, this threshold was $0.35 I_{\text{max}}$ and thus the apparent CDs fed into the FDTD are slightly larger than that would be expected from a more traditional 50% threshold. The binary mask in Fig. 5(a) comes from the “well-patterned die,” while Fig. 5(b) shows a binary mask derived from the “imperfect die.” These two separate dies offer unprogrammed variations in LER, LWR, and line fidelity. The sidewalls of the simulated structures were assumed to be normal. Perspective views of the defects appear in Fig. 6.

From these masks, the LER, LWR, and line fidelity were computed from the middle 80% of the patterned lines. The LER varied among defects within each die. Unplanned imperfections and line breaks in the imperfectly patterned die contributed to the approximate 1-nm increase in LWR

Table 2 Intensity threshold, defect metric, and signal-to-noise (SNR) estimates as the rms roughness, σ_{LER} , of the line edge roughness (LER) increases from 0.65 to 1.95 nm. The defect metric is the summed absolute defect intensity above the intensity threshold. Subvolumes misidentified as defects (“false positives”) and false negatives are marked with an asterisk (*) and do not correspond to an actual defect signal.

σ_{LER} (nm)	Bridge “Bx” $-\theta = 21$ deg, $\phi = 90$ deg			Bridge “By” $-\theta = 21$ deg, $\phi = 0$ deg		
	$4\sigma_1$ Intensity	Def. Int. $> 4\sigma_1$	SNR	$4\sigma_1$ Intensity	Def. Int. $> 4\sigma_1$	SNR
0.65	0.044	3952	18.6	0.069	8585	18.9
0.98	0.053	3817	20.2	0.063	6459	15.5
1.30	0.055	N/A*	N/A*	0.079	9270	8.4
1.63	0.057	1935*	9.7*	0.071	2746*	8.0*
1.95	0.078	2179*	6.9*	0.066	N/A*	N/A*

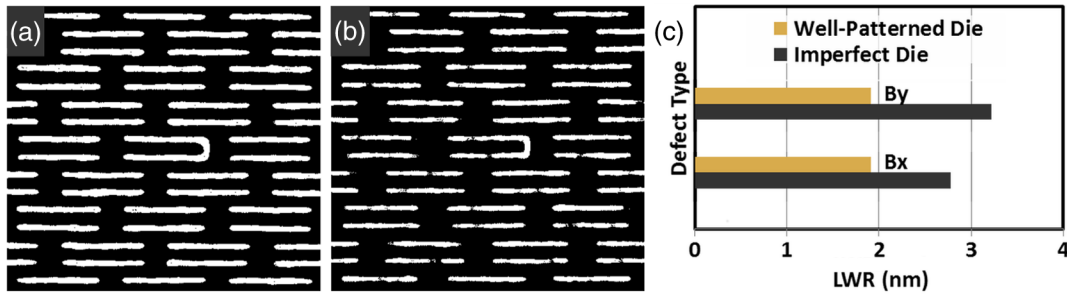


Fig. 5 Comparisons of the simulation inputs for the “well-patterned die” versus the “imperfectly patterned die.” (a) The “By” defect binary mask for the well-patterned die. (b) The “By” defect binary mask for the imperfectly patterned die. (c) Line width roughness (LWR) calculated for the “Bx” and “By” defects.

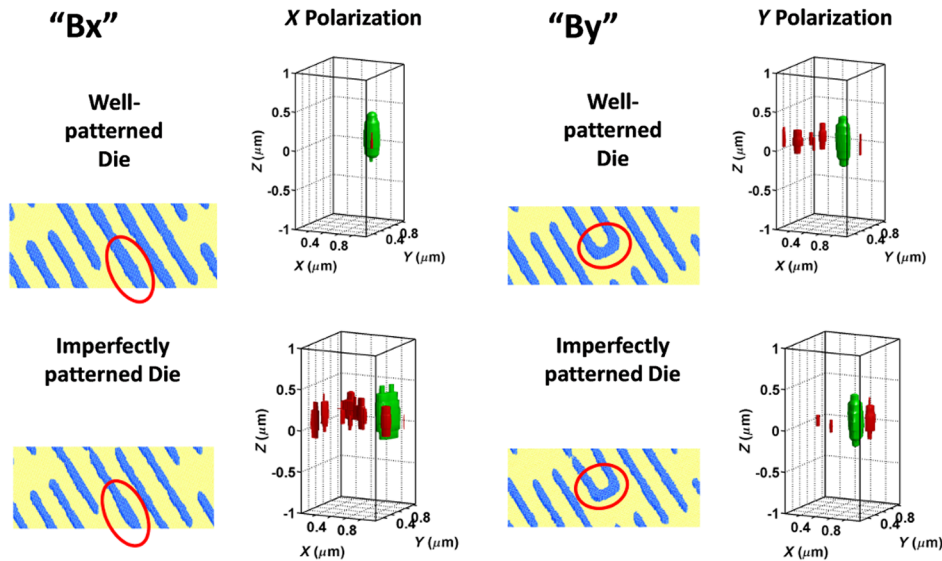


Fig. 6 Differential volumetric analysis of the scattering from two dies and two defect types from the 9-nm gate intentional defect array (IDA) using optimal linear polarizations. Defect SEVD and critical dimension (CD) values are shown in Table 3.

relative to the well-patterned die as shown in Fig. 5(c). The LWR may be difficult to visualize in these panels as the pixel resolution is nominally 2.48 nm/pixel. The continuity of the well-patterned die is nearly 100%, but is as low as 98% for targets on the imperfectly patterned die.

The 2.48-nm SEM pixel resolution provided the lower limit for the cubic FDTD grid size and enabled many more FDTD simulations to be performed relative to the first simulation study, in which a 1.125-nm grid size was used, thus 80 plane waves were simulated to account for the finite aperture of the National Institute of Standards and Technology (NIST) 193-nm microscope.¹¹ The polar angle θ was varied from 11 deg to 45 deg with the entire range of azimuthal angles ϕ simulated to cover the conjugate to the back focal plane of that microscope’s objective lens. Assuming incoherent illumination and Köhler illumination, these several plane wave simulations have been combined to simulate annular illumination for linearly polarized light in Fig. 6 for the two dies and two defects of interest. For this study, the intensity threshold was increased to $I > 5\sigma_1$ in order to isolate a single defect in each volumetric image. As in the first simulation study in the previous subsection, there proved to be a preferential direction for measuring

these defects that corresponded to the alignment of the linear polarization along the axis of the bridge defect. The defect metric, SNR, sphere-equivalent volume diameter (SEVD), and the CDs of the defects simulated are shown in Table 3.

Several trends can be identified from this study. The center z positions of the wafer noise roughly coincide with those of the identified defects. Although there are more wafer subvolumes in the scattering from defects “Bx” on the imperfect die and “By” on the well-patterned die, there is more total intensity in the wafer noise subvolumes for both defects for the imperfect die. Despite similar SEVD values between the two dies per defect, the SNR values are larger for the well-patterned die, especially the “Bx” defect. This defect better illustrates the anticipated difficulties in defect detection as dimensions continue to decrease. The spatial extent along the z -axis from the wafer noise is 500 nm for the imperfect die, comparable with the 700-nm extent of the defect. Although the smaller xyz extent of the wafer noise observed aids in isolating the defects, more sophisticated discriminants against false positives from wafer noise will likely be needed in future evaluations. At present, with volumetric processing, the defect metrics are

Table 3 Defect metric and SNR comparing two dies of differing patterning quality, with the critical dimension (CD) of the defect simulated using finite-difference time-domain (FDTD). Though based on scanning electron microscopy (SEM) measurement, the defect CDs are fixed inputs to the model; the specific SEM intensity threshold used overestimates the CD compared with the SEM CD measurements in Table 4.

	Well-patterned die		Imperfectly patterned die	
	Bridge “Bx”	Bridge “By”	Bridge “Bx”	Bridge “By”
Defect polarization	X	Y	X	Y
Def. Metric	1361	1601	1590	1679
SNR	117.4	32.1	9.8	14.3
SEVD	210 nm	146 nm	203 nm	130 nm
Defect CD	28 nm	26 nm	26 nm	20 nm

comparable between the well-patterned die and the imperfect die, though the SNR values are more favorable for the well-patterned die. These trends will be evaluated experimentally in Sec. 4.

4 Experimental Volumetric Defect Detection

4.1 Comparison of Dies on the SEMATECH 9-nm Intentional Defect Array

Simulation studies have shown that the extra wafer noise is to be expected in the 3-D volumetric analysis of samples with LER and specifically for the imperfectly patterned die. These trends must be confirmed using measurement. In Fig. 2, direct comparison between the imperfectly patterned die and another well-patterned die was hampered by substantially different illumination conditions. In this experiment, “Bx” and “By” defects are measured on two dies on the 9-nm IDA using bright-field illumination using the NIST 193-nm microscope. The full-field effective illumination numerical aperture (NA) is annular due to a catadioptric objective and ranges from $NA = 0.11$ to 0.74 . As discussed in Sec. 1, the “defect” and “reference” volumes are collected sequentially and instrumentation noise effects should be largely mitigated, allowing investigation of the wafer noise.

As shown in Fig. 7, there is more wafer noise from the imperfectly patterned die than from the well-patterned die. In Fig. 7(b), two copies of the “By” defect are clearly identified with the noise subvolumes mostly confined to a narrow z -range. For the same defect on the imperfect die shown in Fig. 7(d), two false positives have been detected and the noise subvolumes are approximately 250 nm in the z extent. For “By,” the xyz extents of the defect signals differentiate the defect from the noise. Contrast this with Figs. 7(a) and 7(c), where the labeled noise subvolumes often are positioned in the same z -range as the intentional defect. From the first simulation study, LER effects did not produce such wafer noise. A number of the noise subvolumes in Fig. 7(c) also have copies due to the shift between the “defect” and “reference” images, thus it is likely that these are unintended defects, such as the line breaks observed by SEM in Fig. 5(b), with intensity noise on par with the scattering from the “Bx” defect. Similar events are less readily observed in Fig. 7(d) due to the relatively large intensity of the “By” defect.

The experimental defect metric and SNR are provided in Table 4. For these experiments, the defect metric is the mean intensity per pixel in the defect subvolume(s). The differences in the defect metrics and SNR for the two “Bx” defects are minimal. Values for the two “By” defects indicate a greater detectability for the imperfectly patterned die. There is a general decrease in the SNR between the second, SEM-based simulation study and the measurement, which indicates that all sources of noise from the samples and instrument have yet to be fully integrated into the simulation.

4.2 Extensibility of Through-Focus Techniques

Bringing this metrology capability from the laboratory to industry is currently an unmet challenge. While the measurements above demonstrate volumetric processing for samples with wafer noise, the added data acquisition required to assemble such volumes is currently impractical for full-time manufacturing process control. In this present work, the time required for a measurement was not optimized and the dataset at left in Fig. 8 is comprised of 47 different z slices. This dataset can be reduced to determine how few slices are required to obtain similar results. In the center and right panels of Fig. 8, the z resolution is reduced to evaluate the effectiveness of volumetric methods with less data.

Varying the z resolution, Δz , from 50 to 300 nm in steps of 50 nm, the number of required slices is reduced from 47 to 8, with each iteration having an SNR comparable with the SNR of the highest resolution with only the $\Delta z = 200$ nm case (not shown) yielding a false positive. Otherwise, only the two copies of the defect were identified.

Given that several images will be necessary to form any volume, at this time volumetric processing may best be applied intermittently. Possibilities include identification of a favorable focal position where defects may be identified with little noise, or application after conventional single-focus inspection to measure a marginally flagged defect more closely before defect review. A commercial tool would have to further optimize image collection time through the z -direction. Possible directions include utilizing several collection paths to obtain images simultaneously at several z -heights^{12,13} or the use of ultrahigh-speed adaptive optics to quickly image along the z -axis.¹⁴ The SNR would

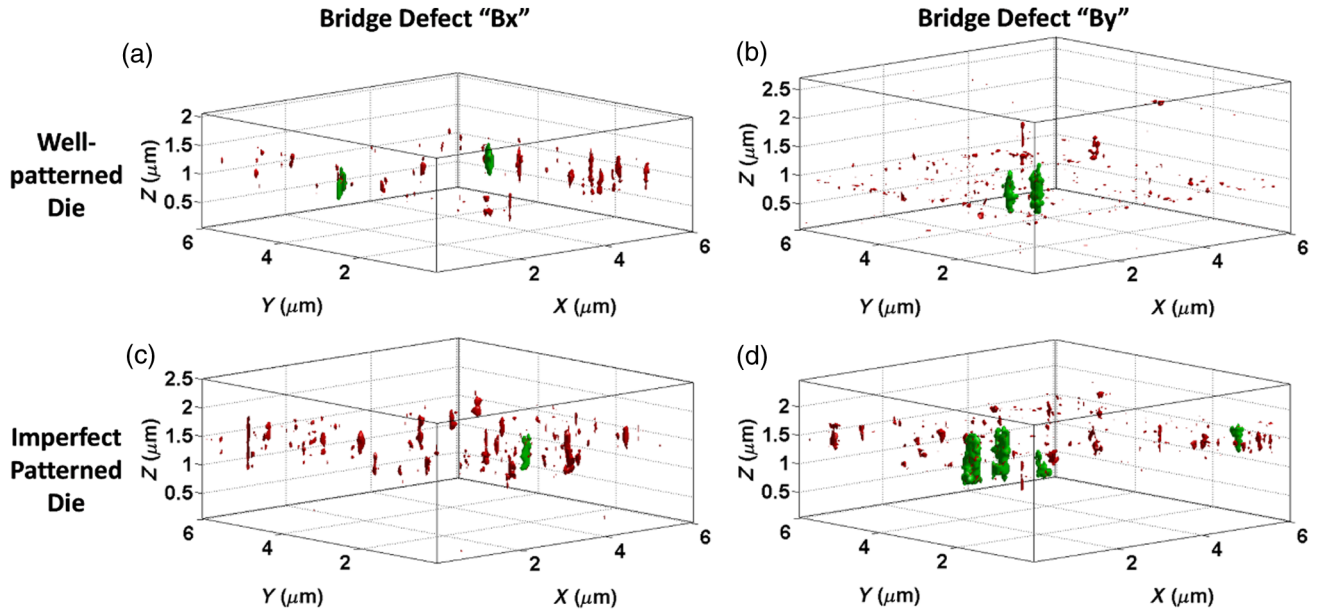


Fig. 7 Experimental differential volumetric defect detection comparing measured intensities from the well-patterned die for defects (a) “Bx” and (b) “By” versus intensities from the imperfectly patterned die for defects (c) “Bx” and (d) “By” on the 9-nm IDA. Thresholds are consistent for a given defect: the “Bx” defect was analyzed using a $7\sigma_i$ intensity threshold with a $160\text{ nm} \times 160\text{ nm} \times 550\text{ nm}$ spatial extent, the “By” defect was analyzed using a $6\sigma_i$ intensity threshold with a $160\text{ nm} \times 160\text{ nm} \times 700\text{ nm}$ spatial extent. In both cases, wafer noise is larger on the imperfectly patterned die.

Table 4 Experimental defect metric and SNR comparing two dies of differing patterning quality, with the CD of the defect as measured using SEM. SEM CD values are averages of the defect’s width as measured between 25% and 75% of its length using a 0.42 normalized intensity threshold where $I_{\min} = 0$ and $I_{\max} = 1$. SEM uncertainties are 1σ values ($k = 1$).

Defect polarization	Well-patterned die		Imperfectly patterned die	
	Bridge “Bx”	Bridge “By”	Bridge “Bx”	Bridge “By”
	X	Y	X	Y
Def. Metric	0.065	0.020	0.059	0.035
SNR	12.5	11.9	10.6	16.1
CD (SEM)	$28 \pm 3\text{ nm}$	$21 \pm 3\text{ nm}$	$23 \pm 2\text{ nm}$	$19 \pm 2\text{ nm}$

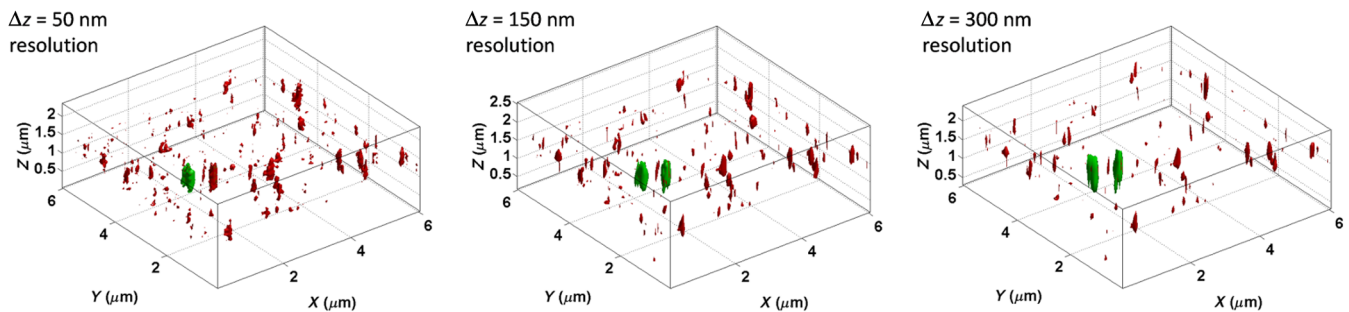


Fig. 8 Measured differential volumetric defect detection as the z resolution is reduced from left to right as shown. Although 3-D filtering and interpolation were performed at the highest z resolution, the intensity and spatial filtering were performed for each new z resolution.

be affected negatively in these fast-scanning techniques, but with decreasing dimensional sizes, the wafer noise may necessitate a new balance among measurement time, SNR, and multiplane image acquisition to maintain yield.

5 Conclusions

Volumetric processing of focus-resolved images can be used to isolate defects in noisy data, as capturing images through focus not only finds an optimal focus for observing defectivity, but also provides additional correlated data. Wafer noise due to the LER, LWR, and variations in the sample may similarly yield correlated data. Simulations show that increased LER is likely to obscure the presence of the defect and that the imperfectly patterned die on the SEMATECH 9-nm IDA would yield lower SNR, and in one case, the z extent of the noise approaches the extent of the defect. In experimental measurements, noise subvolumes did extend through the focal range similarly to the intentional “Bx” defect but this wafer noise is likely due to actual imperfections in the patterning and not changes in LER or LWR.

For most of the data presented, two-dimensional imaging alone could be used for defect detection, and this is preferable for defect detection when accurate. For other cases, however, wafer noise may pervasively frustrate attempts at defect detection through conventional imaging. At several individual z planes, the optical scattering from tolerated patterning imperfections, such as LER, rivals the optical scattering from uncontrolled patterning imperfections, such as bridge defects. As dimensions decrease, the ratio of wafer noise to defect signal may increase, necessitating the image collection at multiple z -heights to overcome wafer noise. Further optical engineering is required, however, for increasing the rate of image collection images of multiple focus planes if volumetric methods are to be applied in an industrial setting.

References

1. International Technology Roadmap for Semiconductors, “2012 tables, Yield enhancement,” 2012, http://www.itrs.net/Links/2012ITRS/2012Tables/Yield_2012Tables.xlsx (13 March 2014).
2. T. F. Crimmins, “Defect metrology challenges at the 11 nm node and beyond,” *Proc. SPIE* **7638**, 76380H (2010).
3. B. M. Barnes et al., “Enhancing 9-nm node dense patterned defect optical inspection using polarization, angle, and focus,” *Proc. SPIE* **8681**, 86810E (2013).
4. B. M. Barnes et al., “Three-dimensional deep sub-wavelength defect detection using $\lambda = 193$ nm optical microscopy,” *Opt. Express* **21**(22), 26219–26226 (2013).
5. T. F. Crimmins, “Wafer noise models for defect inspection,” *Proc. SPIE* **7971**, 79710E (2011).
6. G. D. Evangelidis and E. Z. Psarakis, “Parametric image alignment using enhanced correlation coefficient maximization,” *IEEE Trans. Pattern Anal. Mach. Intell.* **30**(10), 1–8 (2008).
7. A. Taflove, “Application of the finite-difference time-domain method to sinusoidal steady-state electromagnetic-penetration problems,” *IEEE Trans. Electromagn. Compat.* **EMC-22**(3), 191–202 (1980).
8. J. B. Poline et al., “Combining spatial extent and peak intensity to test for activations in functional imaging,” *Neuroimage* **5**(2), 83–96 (1997).
9. A. J. McCann, A. Workman, and C. McGrath, “A quick and robust method for measurement of signal-to-noise ratio in MRI,” *Phys. Med. Biol.* **58**(11), 3775–3790 (2013).
10. International Technology Roadmap for Semiconductors, “2012 tables, Lithography,” 2012, http://www.itrs.net/Links/2012ITRS/2012Tables/Litho_2012Tables.xlsx (13 March 2014).
11. Y. J. Sohn et al., “193 nm angle-resolved scatterfield microscope for semiconductor metrology,” *Proc. SPIE* **7405**, 74050R (2009).
12. P. Prabhat et al., “Simultaneous imaging of different focal planes in fluorescence microscopy for the study of cellular dynamics in three dimensions,” *IEEE Trans. Nanobiosci.* **3**, 237–242 (2004).
13. S. Ram et al., “High accuracy 3D quantum dot tracking with multifocal plane microscopy for the study of fast intracellular dynamics in live cells,” *Biophys. J.* **95**, 6025–6043 (2008).
14. M. Duocastella, B. Sun, and C. B. Arnold, “Simultaneous imaging of multiple focal planes for three-dimensional microscopy using ultra-high-speed adaptive optics,” *J. Biomed. Opt.* **17**, 050505 (2012).

Bryan M. Barnes is a physicist at the National Institute of Standards and Technology. He received his BA degree in mathematics and physics from Vanderbilt University in 1995 and his MS and PhD degrees in physics from the University of Wisconsin-Madison, in 1997 and 2004, respectively. He is the author of more than 40 proceeding and journal papers and holds one patent. His current research interests include optical defect inspection, hybrid metrology, and critical dimension metrology.

Martin Y. Sohn is a physicist at the National Institute of Standards and Technology. He received his BA, MS, and PhD degrees in physics from Yeungnam University, Korea, in 1991, 1993, and 1998, respectively. Before joining NIST, he worked at the Electronics and Telecommunications Research Institute, Korea, as a senior researcher. His research interests include optical metrology for semiconductor manufacturing, advanced optical microscopy, and instrumentation of optical systems.

Biographies of the other authors are not available.